IEEE Access
Multidisciplinary : Rapid Review : Open Access Journal

Received 11 October 2023, accepted 18 November 2023, date of publication 20 November 2023, date of current version 29 November 2023.

Digital Object Identifier 10.1109/ACCESS.2023.3335199

RESEARCH ARTICLE

Imbalanced Bearing Fault Diagnosis Based on RFH-GAN and PSA-DRSN

ZHIDAN ZHONG[1], HAO LIU[1], WENTAO MAO[2], (Member, IEEE), XINGHUI XIE[3], WENLU HAO[4], AND YUNHAO CUI[1]

[1]School of Mechatronics Engineering, Henan University of Science and Technology, Luoyang 471023, China
[2]School of Computer and Information Engineering, Henan Normal University, Xinxiang 453007, China
[3]State Key Laboratory of Aerospace Precision Bearings, Luoyang 471000, China
[4]Luoyang Xinqiang Rotary Bearing Company Ltd., Luoyang 471822, China

Corresponding author: Zhidan Zhong (zzd@haust.edu.cn)

ABSTRACT Bearings in actual working environments typically operate in healthy conditions, resulting in an imbalance in the data collected data. The majority of the collected data are related to bearings in healthy conditions, with insufficient data related to faults. This imbalance leads to accuracy and stability issues in deep learning models used for diagnosis purposes. To address this issue, we propose employing a residual factorized hierarchical search-based generative adversarial network (RFH-GAN) and a residual shrinkage network with pyramidal squeezed attention (PSA-DRSN) for unbalanced fault diagnosis. The process involves transforming vibration signals collected from bearings into time-frequency (TF) domain images through the utilization of the continuous wavelet transform (CWT). The enhanced RFH-GAN generates synthetic fault samples with authentic characteristics, while the PSA-DRSN performs fault diagnosis. The experimental findings substantiate that our method improves the quality of the generated samples, mitigates the data imbalance issues that are inherent in conventional diagnosis methods, and attains heightened precision and efficacy in fault diagnosis tasks.

INDEX TERMS Fault diagnosis, data imbalance, continuous wavelet transform, generative adversarial network, deep residual systolic network.

I. INTRODUCTION

Bearings have widespread use in a variety of fields, including rail transportation, wind power generation, aerospace, and the machinery industry. Nevertheless, the complex operating conditions of rotating machinery lead to inevitable transmission system failures. Bearing failures constitute a significant proportion of these incidents, amounting to 30% to 45% or more of the total failures [1], [2], [3]. The operational performance of rotating machinery is directly influenced by the health statuses of bearings [4]. Severe bearing failures can pose a substantial safety threat to machine operators and reduce the lifespan of machinery. Consequently, precisely and reliably detecting and assessing bearing health statuses [5] are of utmost importance. However, an imbalance in bearing data poses a significant challenge to data-based bearing fault diagnosis methods, often resulting in model bias [6], [7], [8]. Researchers have made significant efforts to address the influence of data imbalance on intelligent bearing fault diagnosis models [9], and their approaches can be employed to mitigate the data imbalance issue.

Approaches based on data augmentation commonly employ generative models or oversampling techniques to increase the number of fault samples, thereby improving the effectiveness of diagnostic models. For instance, Su et al. [10] employed the K-nearest neighbors algorithm to optimize the iterative generation strategy, aiming to enhance the learning efficiency of generative adversarial network (GAN) and achieve high accuracy. Wu et al. [11] obtained enhanced data and achieved high accuracy by applying local weighting to their oversampling technique. Diaz [12] used the synthetic minority oversampling technique (SMOTE) to synthesize fault samples for attaining balanced data while effectively improving the accuracy of fault diagnosis.

The associate editor coordinating the review of this manuscript and approving it for publication was Wei Wei.

Designing classification models using this approach significantly enhances their diagnostic accuracy by crafting models that are specifically customized for limited and imbalanced datasets. To illustrate this point, An et al. [13] presented a self-learning relocatable network (STNN) with the aim of mitigating the impact of imbalanced data on the diagnosis process. This was accomplished by introducing three innovative loss terms: self-belief (L_s), self-suspicion (L_d), and correction (L_e) terms. In a similar vein, Y.W. Tan et al. [14] introduced a domain-adaptive network framework known as deep mixup to tackle distribution mismatches and data imbalance issues. Experimental evidence has demonstrated the effectiveness of this approach in addressing data imbalances. In a different approach, Lu et al. [15] proposed a common feature space mining network (CFCNet), a two-stage migratable network designed to tackle imbalanced fault diagnosis tasks. Additionally, Wu and Zhao [16] presented a DCNN fault classification model that incorporates parameter-based migration learning, yielding promising results.

While the aforementioned methods produced shown promising diagnostic outcomes, they are not without limitations. For example, data augmentation techniques utilizing generative networks such as GANs or VAEs often require a considerable number of samples to effectively capture the underlying data distribution. However, as sample sizes decrease, the quality of the generated samples diminishes, thereby adversely affecting a model's diagnostic accuracy. Similarly, oversampling methods encounter data distribution challenges at the edges, leading to potential impacts on the diagnostic efficacy of the utilized model. Additionally, the design-based approach for classification models heavily relies on researchers' domain expertise, particularly when formulating the loss function, posing challenges in terms of achieving optimal diagnostic outcomes.

To circumvent the aforementioned issues, this paper employs a modified deep residual factorized hierarchical search-based generative adversarial network (RFH-GAN) with superior image processing capabilities to generate fault samples and balance the data. The generated data are subsequently used by a deep residual shrinkage network with pyramidal squeezed attention (PSA-DRSN) for fault diagnosis purposes. The study conducts experiments on various bearing datasets to demonstrate the effectiveness of the proposed approach in terms of addressing data imbalance issues. The method introduced in this research presents several advantages and innovative contributions, which are summarized as follows.

(1) This paper introduces an enhanced approach for diagnosing faults in rolling bearings, leveraging data and feature augmentation techniques to effectively manage imbalanced bearing fault data. By constructing a GAN-based framework to synthesize fault samples and balance their data distribution, the generation quality and stability of the network are improved.

(2) By adopting distinct loss functions for the generators and discriminators of the GAN, the stability of the GAN is enhanced.

(3) To transform vibration signals into TF pictures, the suggested approach employs the CWT. To optimize the ability of the network to create images, this method fully exploits the deep feature information of the RFH-GAN.

(4) A productive pyramidal squeezed attention module is added to enhance the DRSN backbone network. This module enables the network to establish long-term channel dependencies and extract multiscale spatial information with finer levels of detail.

II. THEORETICAL BACKGROUND

A. CONTINUOUS WAVELET TRANSFORM (CWT)

Signal processing frequently entails transforming time domain (TD) signals into TF representations to unveil the most important information. Although TD signals may not always be the optimal representations, methods such as the CWT or the short-time Fourier transform (STFT) are frequently utilized to extract essential information from signals [17].

In this paper, the CWT is selected for transforming TD signals because, in comparison with the Fourier transform, the CWT not only inherits and extends the localization concept of the short-time Fourier transform but also overcomes its limitations, such as the use of a fixed window size for all frequencies [18]. The CWT is defined as follows:

$$CWT_x^{\psi}(\tau, s) = \Psi_x^{\psi}(\tau, s) = \frac{1}{\sqrt{|s|}} \int x(t)\psi(\frac{t-\tau}{s})dt \quad (1)$$

where τ denotes the translation parameter, s denotes the scale parameter, $x(t)$ denotes the TD signals and $\psi(t)$ denotes the mother wavelet function.

One crucial stage in the CWT is the selection of the mother wavelet function, and several options are available, including Gabor, Meyer, Morlet, and other functions [19]. As the Morlet function aligns with the impact characteristics produced by bearing defects [20], it is utilized in this study for the CWT. The Morlet function is defined as follows:

$$\psi(t) = e^{-\frac{t^2}{2}} \cos 5t \quad (2)$$

B. DEEP CONVOLUTIONAL GENERATIVE ADVERSARIAL NETWORK (DCGAN)

The DCGAN represents an improvement over the original GAN [21]. To enhance the image processing capability of the network, the fully connected (FC) network of the original GAN is replaced with a convolutional network, the pooling layer is replaced with a convolutional layer, and BN is employed after the convolutional layer [22]. The Tanh function is utilized in the output layer of the DCGAN generator, while the ReLU activation function is used in the other layers [23]. Conversely, the subsequent layers of the discriminator employ the ReLU function, and the output layer of the discriminator employs the sigmoid function [24].

Fig. 1 shows the DCGAN's generator model, and Fig. 2 shows the DCGAN's discriminator model.

Fig. 3 illustrates the operating principle of the DCGAN. By engaging in an adversarial game between the discriminator and generator, the DCGAN can process images more effectively [25]. The generator receives random noise as its input. The discriminator's role is to determine whether the input samples are real samples by comparing them with the generated samples [26].

The adversarial learning process continues until Nash equilibrium is achieved, thereby reducing the discrepancy between the generated and real samples [27]. At this stage, the generator can produce synthetic samples that closely resemble the distribution of the real samples by utilizing the following loss function for the model:

$$\min_G \max_D V(D, G) = \mathbb{E}_{\mathbf{x}\sim P_r(x)}[\log D(x)] + \mathbb{E}_{\mathbf{z}\sim P_{\mathbf{z}}(z)}[\log(1 - D(G(z)))] \quad (3)$$

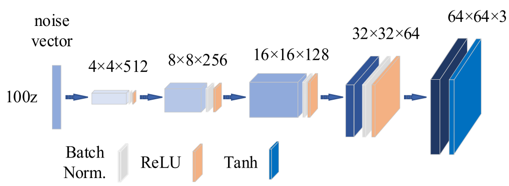

FIGURE 1. Generator model diagram.

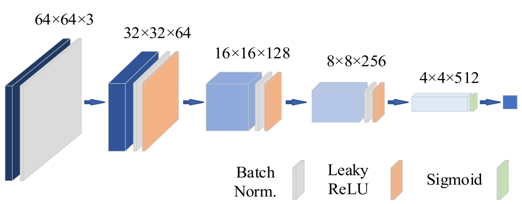

FIGURE 2. Discriminator model diagram.

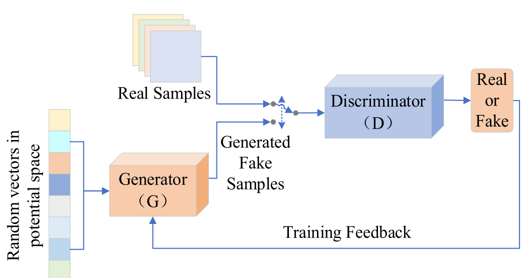

FIGURE 3. Schematic diagram of the DCGAN.

C. DEEP RESIDUAL SHRINKAGE NETWORK (DRSN)

As a deviation from the conventional deep residual network for defect identification, Zhao et al. [28] presented the deep residual shrinkage network (DRSN) in 2020. The DRSN integrates soft thresholding with a neural network architecture to efficiently eliminate noise and generate distinctive features.

Before the emergence of deep learning models, soft thresholding played a crucial role in signal denoising. However, achieving satisfactory denoising performance typically demands substantial filter design expertise [29]. The soft thresholding function is defined as follows:

$$y = \begin{cases} x - \tau & x > \tau \\ 0 & -\tau \le x \le \tau \\ x + \tau & x < -\tau \end{cases} \quad (4)$$

where x represents the input features, y represents the output features and τ represents the threshold value.

Equation (5) presents the derivative of the soft thresholding function, where it can be observed that the derivative of the output with respect to the input can only take values of 0 or 1 to prevent the gradient disappearance and explosion problems [30].

$$\frac{\partial y}{\partial x} = \begin{cases} 1 & x > \tau \\ 0 & -\tau \le x \le \tau \\ 1 & x < -\tau \end{cases} \quad (5)$$

Fig. 4 illustrates the fundamental structure of the residual shrinkage module. The input features undergo absolute value operations and global average pooling before entering the fully connected layer [31]. Equation (6) is employed to normalize the FC layer's output within the range of (0, 1).

$$\alpha_c = \frac{1}{1 + e^{-z_c}} \quad (6)$$

where z_c denotes the cth neuron feature and α_c denotes the cth scaling parameter.

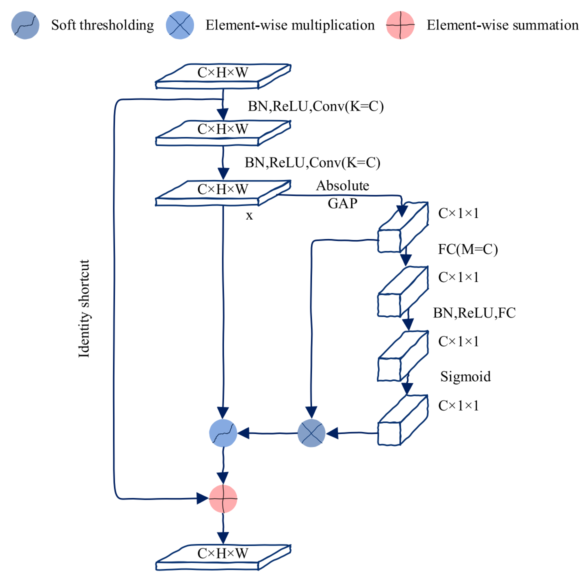

FIGURE 4. Residual shrinkage module.

The threshold value is calculated using Equation (7), where the scaling parameter is multiplied by the threshold value. This prevents the output features from all being zero and allows the soft threshold to be positive and stay within an acceptable range:

$$\tau_c = \alpha_c \cdot \underset{i,j}{\text{average}} \left| x_{i,j,c} \right| \tag{7}$$

where τ_c denotes the threshold value of the cth channel of the feature map;$|\cdot|$ denotes the absolute value operation; and i, j and c represent the width, height, and channel indices of feature map x, respectively.

III. PROPOSED METHOD

A. RFH-GAN-BASED FAKE SAMPLE GENERATION

1) LOSS FUNCTION OF THE RFH-GAN

The inherent instability of a GAN has been well established [32]. The objective of the generator is to minimize the Jensen–Shannon (JS) index, striving to maximize the similarity between the distributions of the real and generated data. This enables the generator to produce data with a distribution closely resembling that of the actual samples [33]. However, when there is no overlap between the true and model distributions, the use of the JS divergence measure results in zero outputs from the optimal discriminator for all generated data [34]. Consequently, the gradient disappears, leading to instability during the training process of the GAN. The JS index is defined as:

$$JS\left(P_r \| P_g\right) = \frac{1}{2} D_{KL}\left(P_r \| P_m\right) + \frac{1}{2} D_{KL}\left(P_g \| P_m\right) \tag{8}$$

$$P_m = \frac{1}{2}\left(P_r + P_g\right) \tag{9}$$

where P_g denotes the distribution of the generated data, P_r denotes the distribution of the real data, and $D_{KL}(\cdot)$ denotes the Kullback–Leibler (KL) divergence.

The utilization of separate loss functions for the generator and discriminator improves the quality of the generated images and enhances the stability of the GAN training process. Utilizing the least-squares loss function [35] can lead to a more stable generator training procedure. The least-squares loss function is more effective at addressing the issue of gradient disappearance during generator training than the conventional cross-entropy loss function.

In contrast to the JS measure employed in the original GAN, the Wasserstein distance can be utilized as a discriminator loss function [36], and its optimization process is more reliable. By computing the dissimilarity between the distributions of the generated and genuine data, the Wasserstein distance generates a loss signal characterized by smoothness and continuity, thereby aiding in mitigating concerns such as modal collapse [37]. Equation 10 presents the expression of the Wasserstein distance:

$$W\left(P_r, P_g\right) = \inf_{\gamma \in S(P_r, P_g)} E_{(x,y)\sim\gamma}[\|x - y\|] \tag{10}$$

where inf denotes the maximum lower bound, γ denotes the joint distribution of P_r and P_g, $S(P_r, P_g)$ denotes all possible joint distributions, and $\gamma(x, y)$ denotes the "cost" of transferring from x to y.

To further enhance the stability of the training process, we introduce a human gradient penalty term [38]. By assigning a gradient penalty to the linearly interpolated samples between the real and fake samples, the gradient penalty term might encourage the discriminator to be attentive to smooth changes in the sample space. This improves the quality and diversity of the fake samples and enhances the training stability of the GAN. The objective functions of the enhanced GAN are as follows:

$$\min_G V(G) = \frac{1}{2}\mathbb{E}_{\mathbf{z}\sim p_{\mathbf{z}}(z)}\left[(D(G(z)) - 1)^2\right] \tag{11}$$

$$\max_D V(D) = \mathbb{E}_{\mathbf{x}\sim P_r(x)}\left[D(x)\right] - \mathbb{E}_{\mathbf{z}\sim P_{\mathbf{z}}(z)}[D(G(z))] + G_p \tag{12}$$

$$\hat{x} = \epsilon x + (1 - \epsilon)G(z) \tag{13}$$

$$G_p = \lambda \cdot \mathbb{E}_{\hat{\mathbf{x}}\sim P_{\hat{\mathbf{x}}}}\left[\left(\left\|\nabla D(\hat{x})\right\|_2 - 1\right)^2\right] \tag{14}$$

where $\hat{x}$ denotes the linear interpolation operation between the discriminator input and the true sample, λ denotes the weight of the gradient penalty term, ∇ denotes the gradient operator, G_p represents the gradient penalty, ϵ stands for a real number in the range [0,1], and $\|\cdot\|_2$ denotes the L_2 parametrization of a vector.

2) GENERATOR STRUCTURE OPTIMIZATION

Similarly, to address the issue of training instability in GANs, we incorporate a residual network module into the generative network, enabling the fusion of the features learned by the higher-level network [39].

The proposed residual generative adversarial network optimizes the feature transfer operations between different neural network layers by adding inputs and mappings at the output of each hidden layer. The proposed residual generative adversarial network is composed of five residual network layers. Additionally, the model architecture is depicted in Fig. 5.

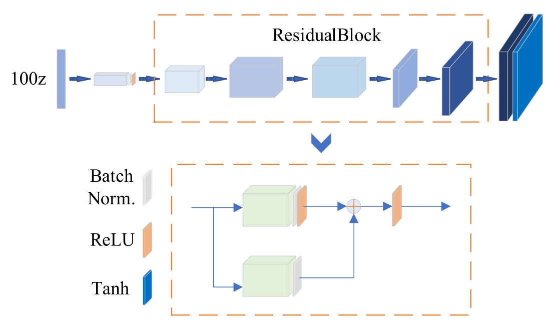

FIGURE 5. Structural illustration of the residual generation model.

3) DISCRIMINATOR STRUCTURE OPTIMIZATION

The network structure of the discriminator is inspired by MnasNet, and a decomposed hierarchical search space is integrated into the discriminator to achieve hierarchical diversity. In this method, the CNN model is divided into discrete blocks, the input resolution is gradually decreased, the filter size is increased, and separate searches are carried out for the operations and connections in each block. This enables the use of various layer structures in various blocks [40]. The strategy ensures layer diversity and boosts the computational efficiency of the network by lowering the number of required parameters. Fig. 6 shows the enhanced discriminator structure, while Fig. 7 shows the phase layer structure.

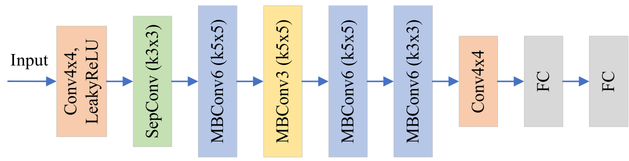

FIGURE 6. Architecture of the discriminator.

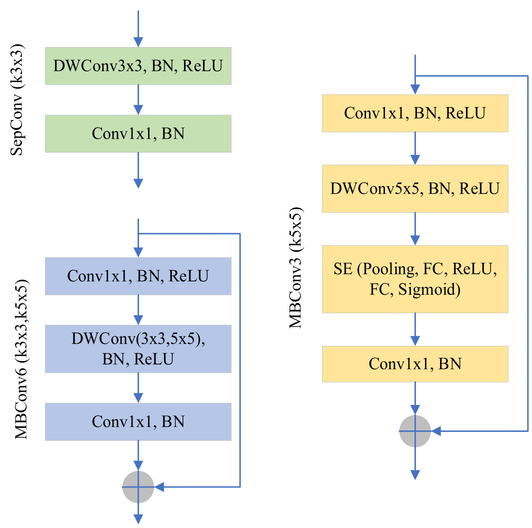

FIGURE 7. The layer configuration of the discriminator. "MBConv" represents mobile inverted bottleneck convolution, and "DWConv" signifies depthwise convolution.

B. FAULT CLASSIFICATION BASED ON THE PSA-DRSN

The PSA-based residual shrinkage block and the architecture of the pyramidal squeezed attention-based deep residual shrinkage network (PSA-DRSN) introduced in this paper are depicted in Fig. 8 and Fig. 9, respectively.

The PSA module, depicted in Fig. 10, employs a multiscale pyramidal convolution structure to combine the information acquired from the input feature maps [41]. Initially, the PSA module constructs a multiscale feature map using the proposed squeeze-and-concatenation (SPC) technique, as depicted in Fig. 11. The relationship can be formulated as follows:

$$G = 2^{\frac{K-1}{2}} \tag{15}$$

where K represents the nucleus size and G represents the group size.

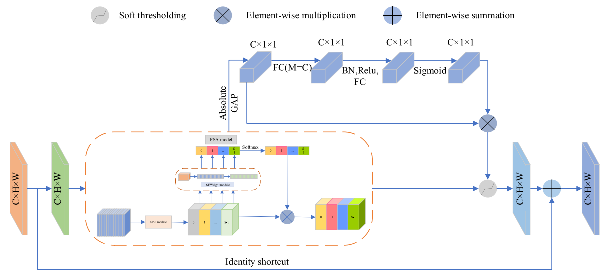

FIGURE 8. PSA-based residual shrinkage block (PSA-RSB).

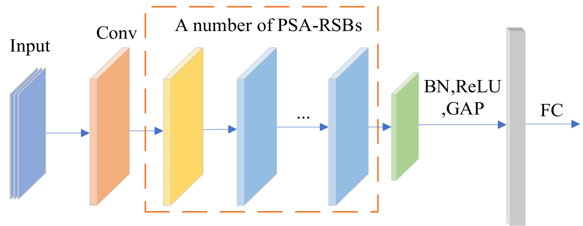

FIGURE 9. Architecture of the PSA-DRSN model.

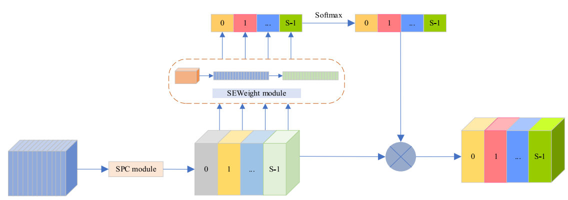

FIGURE 10. Architecture of the PSA module.

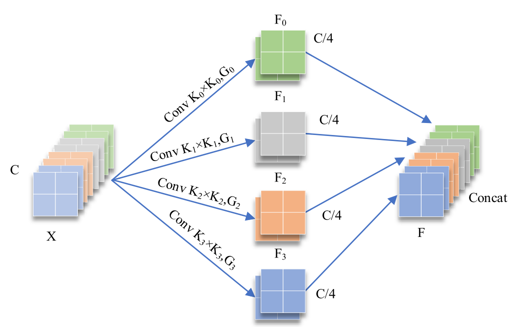

FIGURE 11. The SPC module, where C denotes the input channel dimensions of each branch, and each feature map at different scales of Fi has a common channel dimensionality of C' = C/S with S=4. Concat denotes connecting features in the channel dimension.

The equation defining the generation of the multiscale feature map is as follows:

$$F_i = Conv\,(k_i \times k_i, G_i)\,(X) \quad i = 0, 1, 2 \cdots S-1 \tag{16}$$

where $k_i = 2 \times (i+1) + 1$ denotes the ith kernel size, G_i denotes the ith group size, and F_i signifies the feature maps at distinct scales.

The multiscale preprocessed feature maps are obtained as shown in the following equation:

$$F = Cat\,([F_0, F_1, \cdots, F_{S-1}]) \tag{17}$$

Channel-level attention vectors are obtained through the utilization of the SEWeight module for attention extraction, yielding attention weights that can be represented as a vector:

$$Z_i = SEWeight\left(F_i\right), \quad i = 0, 1, 2 \cdots S-1 \tag{18}$$

where Z_i represents the attention weights.

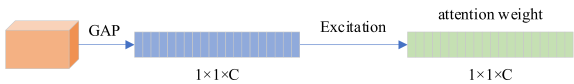

FIGURE 12. SEWeight module.

To facilitate the interaction of attention information, we fuse the cross-dimensional vectors. The complete multiscale channel attention vector is obtained sequentially as outlined below:

$$Z = Z_0 \oplus Z_1 \oplus \cdots \oplus Z_{S-1} \tag{19}$$

where the concatenation operator is denoted by $\oplus$, Z_i represents the attention value originating from the F_i, and Z signifies a vector comprising multiscale attention weights.

Second, the recalibration weights of the multiscale channels are acquired by recalibrating the channel-level attention vectors using the softmax function, as shown in the following equation:

$$\text{att}_i = Soft\max\left(Z_i\right) = \frac{\exp\left(Z_i\right)}{\sum_{i=0}^{S-1} \exp\left(Z_i\right)} \tag{20}$$

where att_i is the weight of the multiscale channel recalibration operation. The channel attention of the feature recalibration process is stitched and fused to obtain the whole channel attention vector as follows:

$$att = att_0 \oplus att_1 \oplus \cdots \oplus att_{S-1} \tag{21}$$

where att is the multiscale channel weight obtained after noticing the interaction.

Finally, multiplying the rescaled weights of the multiscale channel attention att_i with the feature map of the corresponding scale F_i yields a refined feature map with richer multiscale feature information, which can be expressed as:

$$Y_i = F_i \odot att_i \quad i = 1, 2, 3, \cdots S-1 \tag{22}$$

C. UNBALANCED FAULT DIAGNOSIS BASED ON THE RFH-GAN AND PSA-DRSN

This study introduces a novel fault diagnosis approach that integrates an RFH-GAN and a PSA-DRSN to tackle the data imbalance issue in fault diagnosis cases. The RFH-GAN is trained to adaptively learn the data distribution and generate fault samples to construct balanced data. However, the generated samples inevitably contain noisy or redundant features. To mitigate the impact of noise or redundant features on the deep learning-based diagnosis results, this paper employs the PSA-DRSN. The PSA-DRSN learns effective discriminative features from noise-containing data or more complex data to achieve enhanced diagnosis accuracy and stability. The specific process of this method is illustrated in Fig. 13.

(1) Data preprocessing is performed. The TD signals are first truncated using a sliding window, as depicted in (a) of Fig. 14. The truncation window covers M data units at once, where each unit represents a complete cycle. After each intercept, the window is shifted backward by N units. Subsequently, the CWT is applied to convert the signals into a TF image. This process is iterated until reaching the end, as illustrated in (b) of Fig. 14.

(2) The generative network is trained using the TF images generated by the CWT, and the generator is used to generate fault samples after the training process is completed.

(3) The CWT-transformed normal samples are partitioned into training and test sets at an 8:2 ratio. The test set for the fault category contains an equal number of samples to that contained in the test set for the normal category. The generator is exclusively incorporated into the training set to produce fault samples.

(4) The PSA-DRSN is trained using the training and test sets to assess the model's performance. The model's effectiveness is evaluated through metrics such as the recall and F1 values.

IV. EXPERIMENT

A. VALIDATION USING THE CWRU DATASET

1) DATASET DESCRIPTION AND TRANSFORMATION

We utilized the CWRU bearing dataset, encompassing four distinct bearing health conditions: normal, inner fault (IF), outer fault (OF), and rolling element failure (RF). The dataset was established under four distinct operational conditions, as depicted in Table 1. The experimental data were segregated into two sections, fans and drive ends, with sampling frequencies of 12 kHz and 48 kHz, respectively. The experiments were performed using the drive-side data with a sampling frequency of 12 kHz. To provide comprehensive representations of the bearings' statuses while accounting for various types of bearing faults, fault sizes, and operating conditions, the bearings were categorized into 10 types based on their fault types and sizes, as detailed in Table 2.

TABLE 1. Four distinct operational scenarios.

Rotational speed (rpm)	Load (hp)	Working condition
1797	0	C_0
1772	1	C_1
1750	2	C_2
1730	3	C_3

Fig. 15 illustrates the TD waveforms of various health states. The TD diagrams clearly show that vibration data in the normal state are characterized by a smooth profile with minor amplitude fluctuations. Conversely, under faulty conditions, notable shocks and burrs are observed in the TD waveforms, with the amplitudes of shocks increasing in

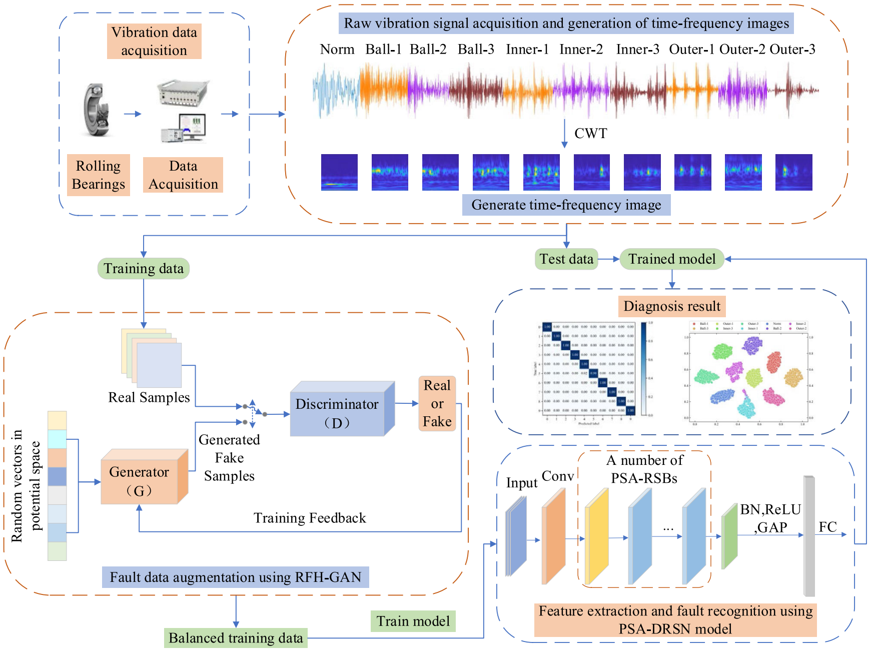

FIGURE 13. Experimental flowchart.

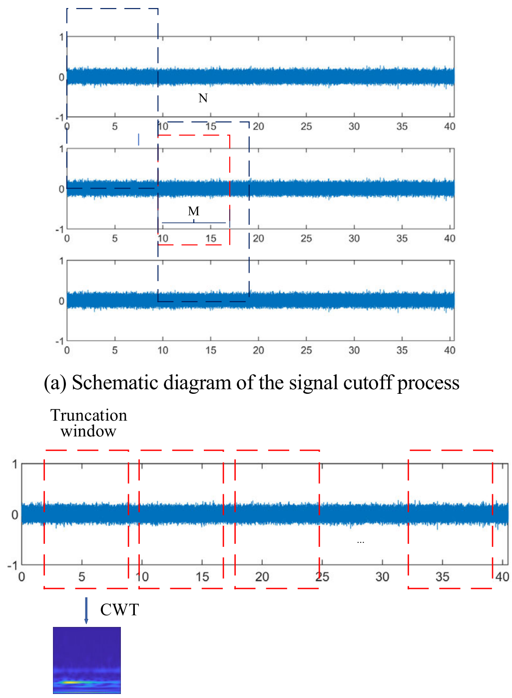

(a) Schematic diagram of the signal cutoff process

(b) Schematic diagram of the CWT process

FIGURE 14. Schematic diagrams of the vibration signal truncation and conversion processes.

TABLE 2. Dataset description.

Fault location	Damage type	Label	Fault diameter/in	Original sample size
Normal	Norm	0	/	3600
Ball	Ball-1	1	0.007	1192
	Ball-2	2	0.014	1193
	Ball-3	3	0.021	1193
Inner raceway	Inner-1	4	0.007	1195
	Inner-2	5	0.014	1192
	Inner-3	6	0.021	1193
Outer raceway	Outer-1	7	0.007	1193
	Outer-2	8	0.014	1193
	Outer-3	9	0.021	1196

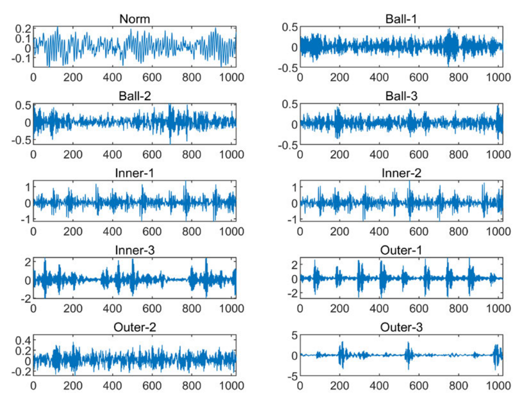

FIGURE 15. TD waveforms of vibration data obtained under various health conditions.

the majority of the fault vibration data as the bearing fault severity rises.

Fig. 16 showcases the TF images extracted from the TD data of the CWRU dataset after performing CWT processing. These images portray the various states, including the normal, rolling body failure, inner fault, and outer fault states. Discrepancies in the TF attributes across distinct health states are discernible from the illustration. More specifically, the

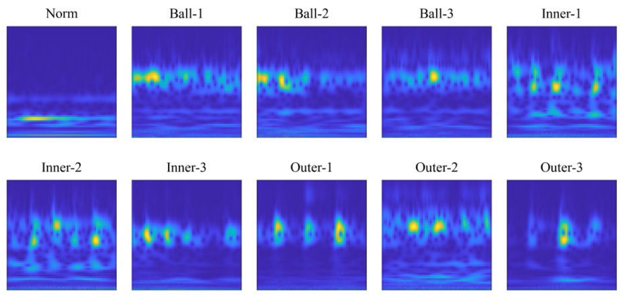

FIGURE 16. TF images derived through the application of the CWT to vibration data representing distinct health conditions.

TF images of the normal state display relatively consistent and smooth attributes, whereas those corresponding to faulty states manifest substantial alterations across both the time and frequency domains. Noteworthy peaks and irregular patterns characterize these alterations, and the amplitudes of these attributes typically escalate with the severity of the bearing fault.

Fig. 17 illustrates a comparative analysis between the initial TF images and their generated counterparts across three distinct health conditions.

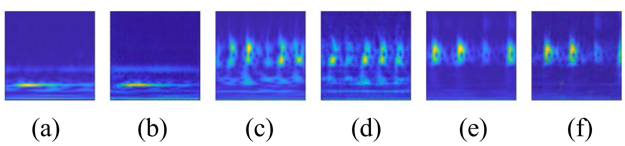

FIGURE 17. Original and generated images depicting various health conditions: (a) original image in the normal state; (b) generated image in the normal state; (c) original image of an inner fault; (d) generated image of an inner fault; (e) original image of an outer fault; and (f) generated image of an outer fault.

We assessed the obtained samples' Fr'echet inception distance (FID) and maximum mean discrepancy (MMD) values. Two DA methods, a WGAN and a DCGAN, were also tested. In each experiment, 60 TF images were chosen at random, and only samples of this kind were used to explicitly train the model. The experimental setups and outcomes of the various DA approaches are described in Table 3. The training period was set to 400 for the WGAN, DCGAN, and RHF-GAN.

TABLE 3. Experimental setups and outcomes of different DA approaches.

Method	FID	MMD
WGAN	0.891	1.019
DCGAN	0.893	1.023
RFH-GAN	0.674	0.956

2) DATASET SETUP AND RESULTS ANALYSIS

In practical engineering scenarios, the amount of data collected during the normal operations of rolling bearings is typically significantly greater than the amount of fault data [42]. To assess the effectiveness of the proposed model in terms of addressing imbalanced data, it is crucial to replicate the real-world engineering context, where the amount of data collected during normal rolling bearing operations greatly surpasses the amount of faulty data. However, substantial data disparities can readily constrain the classification precision of the utilized fault diagnosis method. Consequently, this study established four imbalanced datasets and one balanced dataset to mirror the authentic engineering setting. The balanced dataset employed synthesized samples to augment the fault data, whereas the imbalanced dataset's samples were randomly drawn from the original dataset. The ratio of normal samples to fault samples and their respective quantities are detailed in Table 4.

TABLE 4. Datasets with different proportions.

Fault location	Data proportion			
	1:1	3:1	10:1	30:1
Normal	3600			
Ball	3600	1200	360	120
Inner raceway	3600	1200	360	120
Outer raceway	3600	1200	360	120

In this experimental setup, which is characterized by an imbalanced dataset, a comprehensive performance comparison involving the proposed model was conducted using evaluation metrics, including the F1 value, recall, precision, and a confusion matrix.

Fig. 18 illustrates that a reduction in the number of fault samples results in diminished diagnostic performance for the model. Conversely, an augmentation in the number of fault samples leads to an enhancement in the model's diagnostic performance, accompanied by accelerated convergence. Generally, the diagnostic outcomes ameliorate with the upsurge in the sample count. The collective findings obtained from the five experiments are consolidated in Table 5.

TABLE 5. Diagnostic accuracies achieved on different datasets.

Evaluation indicators	Data proportion 1:1	3:1	10:1	30:1
F1 score	99.74%	99.12%	98.78%	93.42%
Recall	99.74%	99.13%	98.77%	94.05%
Precision	99.75%	99.15%	98.09%	94.51%

To evaluate the viability and feasibility of the suggested method, we employed diverse deep learning models for training on the datasets. Subsequently, the diagnostic outcomes of the proposed method were juxtaposed with those obtained from the previously developed models. The diagnostic findings obtained from various procedures are contrasted in Table 6.

To offer a more intuitive portrayal of the diagnostic outcomes obtained across diverse datasets, we employed t-SNE to reduce the dimensionality of the output layer for the PSA-DRSN test set. The ensuing results were then visually presented, as depicted in Fig. 20. The figure elucidates that as the number of samples increases, the sample features

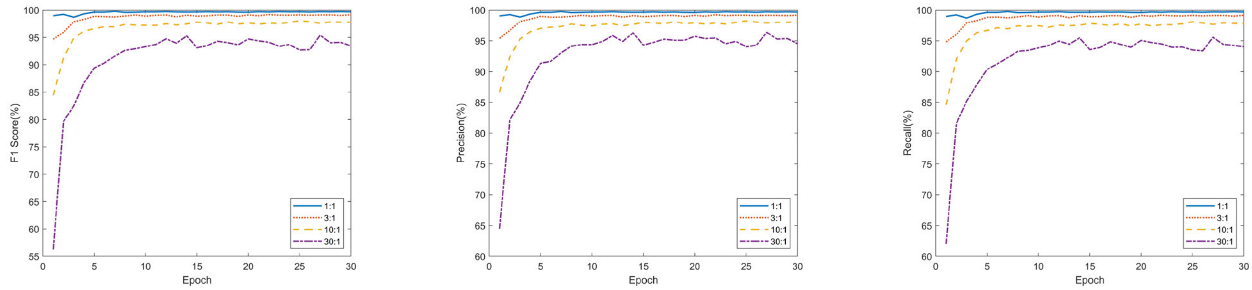

(a) (b) (b)

FIGURE 18. F1 value, precision and recall variation curves.

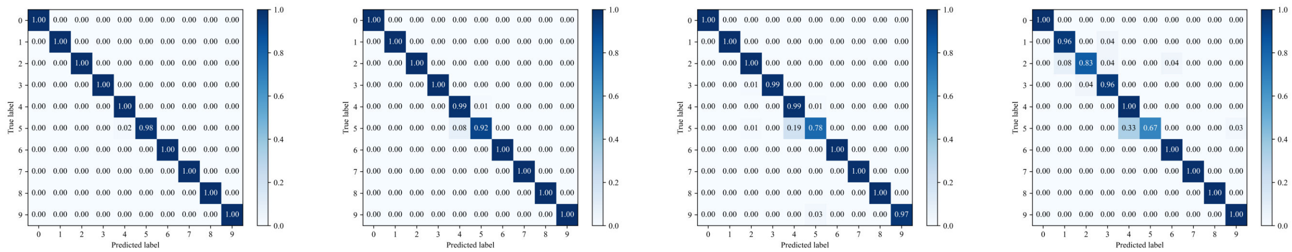

(a) 1:1 (b) 3:1 (c) 10:1 (d) 30:1

FIGURE 19. Confusion matrices of the diagnostic results obtained on different datasets.

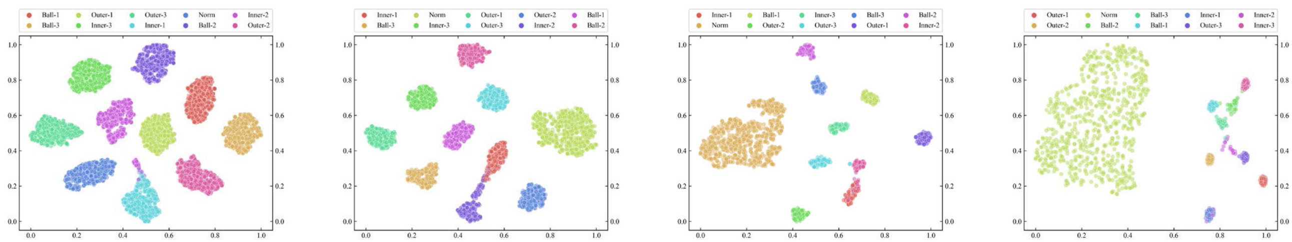

(a) 1:1 (b) 3:1 (c) 10:1 (d) 30:1

FIGURE 20. Feature visualizations produced via t-SNE.

TABLE 6. Outcomes of various approaches.

Models	Data proportion 1:1	3:1	10:1	30:1
PSA-DRSN	99.74%	99.12%	98.78%	93.42%
DRSN	99.13%	98.24%	98.01%	92.19%
ConvNext-T	98.89%	97.68%	97.76%	92.01%
ResNet18	97.23%	96.24%	96.38%	91.39%
CNN	96.35%	95.18%	94.86%	90.61%

become more discernible. This observation implies the effectiveness of the proposed approach in terms of mitigating data imbalance concerns, ultimately enhancing the precision and robustness of the diagnostic model [43].

B. VALIDATION USING THE PADERBORN UNIVERSITY DATASET

1) DATASET DESCRIPTION AND TRANSFORMATION

For this experimental study, a bearing dataset from Paderborn University, obtained from a dedicated bearing test bench, was utilized. The experimental dataset was produced by introducing rolling bearings with varying damage types into a bearing test module. All bearings employed in the experiment belonged to the 8-body rolling category, designated 6203. The defective bearings were categorized into two classes: artificial damage and real damage. Artificial damage entailed EDM (cracking), drilling (spalling), and utilization of an electric engraving machine (pitting), whereas real damage bearings were derived from an accelerated life test bench. The dataset was established under four distinct operational conditions, each entailing three environmental variables, as depicted in Table 7.

The Paderborn bearing dataset was sampled at a frequency of 64 kHz and encompassed three health conditions: normal, inner faults, and outer faults. The faulty data employed in the experiments originated from genuine damage data acquired through accelerated life tests. A total of 15 datasets were harnessed, each encompassing 20 sets of raw data across four distinct operational scenarios, as elaborated in Table 8.

TABLE 7. Four distinct operational scenarios.

Rotational speed (rpm)	Load torque (Nm)	Radial force (N)	Working condition
1500	0.7	1000	W_0
900	0.7	1000	W_1
1500	0.1	1000	W_2
1500	0.7	400	W_3

TABLE 8. Experimental dataset descriptions.

Fault location	Fault category	Label	Dataset number	Original sample size
Normal	Norm	0	K001, K002, K003, K04, K005	1800
Inner raceway	Inner Fault	1	KI04, KI14, KI16, KI18, KI21	600
Outer raceway	Outer Fault	2	KA04, KA15, KA16, KA22, KA30	600

The TD waveforms representing distinct health conditions are depicted in Fig. 21. For illustration purposes, a sample from operational condition W0 was randomly chosen for the health state dataset K001, whereas for the inner fault dataset and the outer fault dataset, the single-point damage datasets KI04 and KA04, respectively, were employed.

Fig. 21 depicts that in the healthy state, the vibration signal manifests as a smooth, stochastic waveform. Conversely, the inner and outer fault states showcase a pronounced rise in amplitude, which is characterized by substantial periodic or irregular shock and burr signals.

Fig. 22 depicts the TF images derived from the Paderborn dataset's TD data after performing the transformation. These images portray the normal, inner fault, and outer fault conditions. Evidently, distinct health conditions exhibit discernible TF characteristics, as seen in the figure.

Fr'echet inception distance (FID) and maximum mean discrepancy (MMD) values were computed for the acquired samples. Three domain adaptation (DA) techniques, namely, the WGAN, DCGAN, and RHF-GAN, were employed. Each trial exclusively utilized samples of this type, selecting 60 random TF images. This explicit training approach is elaborated in Table 9, providing an overview of the experimental configuration and the outcomes of distinct DA techniques. A training duration of 400 iterations was applied for the WGAN, the DCGAN, the RHF-GAN, and their combined implementation.

TABLE 9. Experimental setups and outcomes of different DA approaches.

Method	FID	MMD
WGAN	0.828	1.083
DCGAN	0.831	1.126
RFH-GAN	0.792	1.043

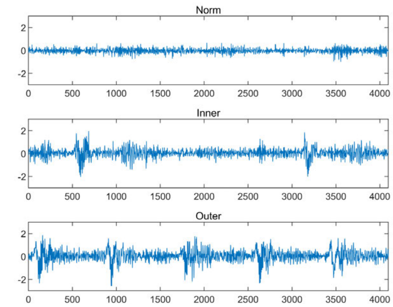

FIGURE 21. TD waveforms depicting vibration data across distinct health conditions.

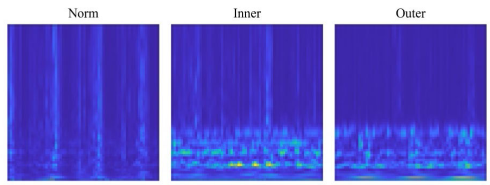

FIGURE 22. TF images extracted from vibration data across various health conditions.

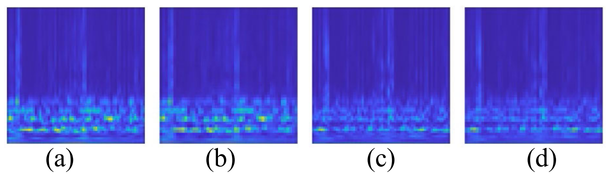

FIGURE 23. Original and generated images representing various health conditions: (a) original inner fault image; (b) generated inner fault image; (c) original outer fault image; and (d) generated outer fault image.

2) DATASET SETUP AND RESULTS ANALYSIS

In Experiment 2, we generated three unbalanced datasets and one balanced dataset. The balanced dataset was augmented with the generated samples to complement the faulty samples, whereas the unbalanced dataset consisted of randomly chosen samples from the original dataset. Table 10 outlines the ratio of normal samples to each type of faulty sample and the corresponding sample counts.

TABLE 10. Datasets with different proportions.

Fault Category	Data proportion			
	1:1	3:1	10:1	30:1
Normal	1800	1800	1800	1800
Inner Fault	1800	600	180	60
Outer Fault	1800	600	180	60

Fig. 24 demonstrates the enhancement in the model's diagnostic performance as the number of fault samples escalates. Furthermore, with a larger number of fault samples, the model exhibits accelerated convergence and attains improved final outcomes. The average of the final results obtained from the five conducted experiments is presented in Table 11.

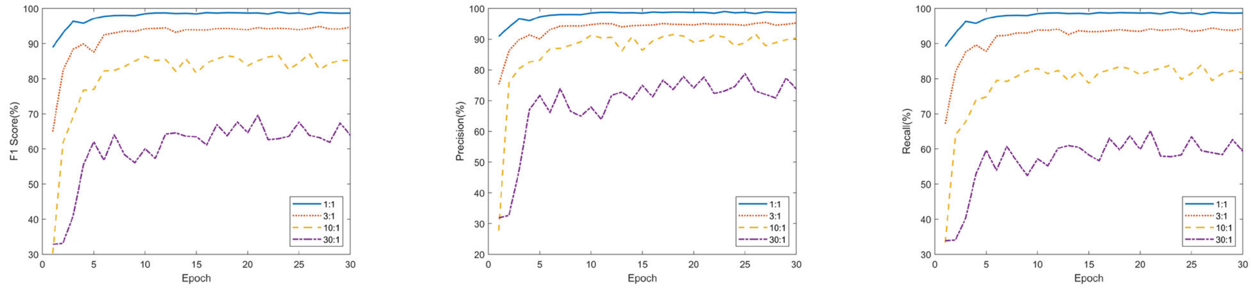

(a) (b) (c)

FIGURE 24. F1 value, precision and recall variation curves.

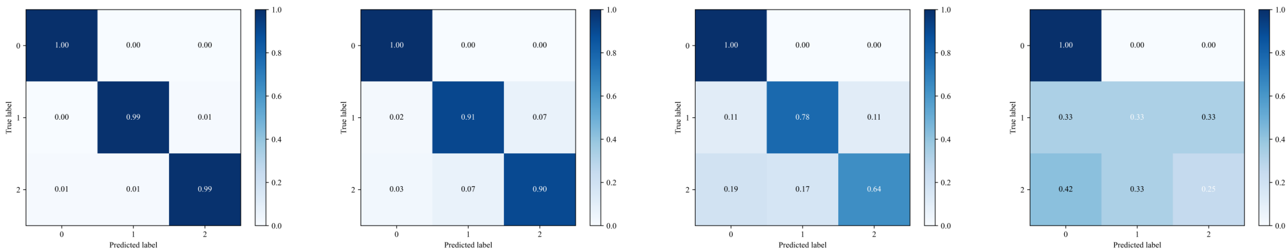

(a) 1:1 (b) 3:1 (c) 10:1 (d) 30:1

FIGURE 25. Confusion matrices produced for the Paderborn dataset.

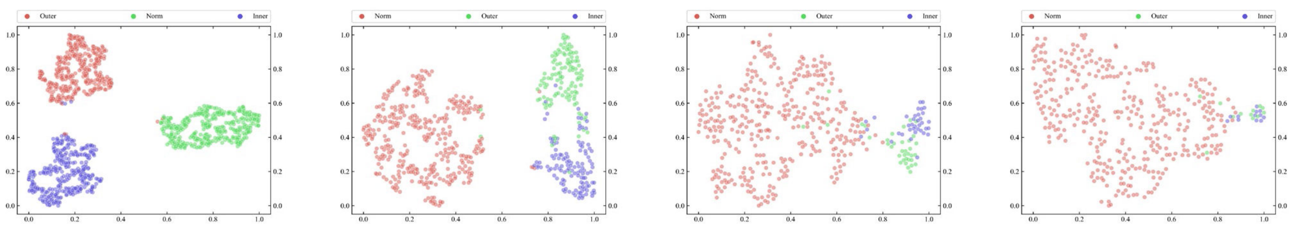

(a) 1:1 (b) 3:1 (c) 10:1 (d) 30:1

FIGURE 26. Feature visualizations produced via t-SNE.

TABLE 11. Diagnostic accuracies achieved on different datasets.

Evaluation indicators	Data proportion 1:1	3:1	10:1	30:1
F1 score	99.49%	94.85%	89.76%	67.77%
Recall	98.11%	94.25%	85.66%	61.40%
Precision	98.12%	95.29%	89.05%	80.14%

TABLE 12. Outcomes of various approaches.

Model	Data proportion 1:1	3:1	10:1	30:1
PSA-DRSN	99.49%	94.85%	89.76%	67.77%
DRSN	98.62%	94.14%	88.62%	66.19%
ConvNext-T	98.44%	93.83%	88.11%	65.84%
ResNet18	98.39%	93.24%	87.83%	64.86%
CNN	98.37%	92.89%	87.44%	63.73%

We trained on the dataset using various deep learning models to validate the effectiveness of the suggested approach. The proposed method's diagnostic outcomes were compared with those of the aforementioned models. The F1 scores yielded by various techniques are displayed in Table 12.

As illustrated in Fig. 25, the comparison among confusion matrices produced across diverse datasets highlights the enhancement in the model's classification capability provided by the proposed method, effectively augmenting the diagnosis stability and accuracy of the model.

Within this study, t-SNE was employed for dimensionality reduction to visualize the results obtained by the output layer of the PSA-DRSN on the test set, as depicted in Fig. 26. The illustration highlights that with heightened sample balance, the sample features display enhanced differentiation and separation. This observation underscores the efficacy of the proposed method in terms of mitigating data imbalance concerns, consequently augmenting the precision and stability of the diagnostic model [43].

V. CONCLUSION

This paper presents an intelligent method for diagnosing bearing faults in the presence of data imbalance by utilizing an RFH-GAN and a PSA-DRSN. The proposed approach involves preprocessing the original signals using the CWT to extract TF features enriched with fault-related information. Subsequently, the RFH-GAN algorithm is deployed to automatically learn the distribution of the input data and generate additional fault samples for balancing the dataset. Finally, fault diagnosis is performed using the PSA-DRSN. Experimental results substantiate the efficacy of the proposed method in terms of effectively managing fault data with varying degrees of imbalance, resulting in improved performance.

Nonetheless, the suggested approach exhibits certain limitations. First, its reliance on high-quality vibration signals for generating TF images renders its effectiveness susceptible to compromised data quality. Second, the model training process is tailored to a specific bearing type, potentially inhibiting its generalization to alternative bearings or analogous mechanical configurations. As a result, forthcoming research endeavors will center around enhancing the efficacy of the proposed approach and broadening its adaptability to encompass diverse bearing types or similar mechanical systems, with a particular emphasis on scenarios characterized by suboptimal data quality.

REFERENCES

[1] K. Zhang, C. Fan, X. Zhang, H. Shi, and S. Li, "A hybrid deep-learning model for fault diagnosis of rolling bearings in strong noise environments," *Meas. Sci. Technol.*, vol. 33, no. 6, Jun. 2022, Art. no. 065103.

[2] D.-T. Hoang and H.-J. Kang, "Rolling element bearing fault diagnosis using convolutional neural network and vibration image," *Cognit. Syst. Res.*, vol. 53, pp. 42–50, Jan. 2019.

[3] Z. Chen, Y. Liao, J. Li, R. Huang, L. Xu, G. Jin, and W. Li, "A multi-source weighted deep transfer network for open-set fault diagnosis of rotary machinery," *IEEE Trans. Cybern.*, vol. 53, no. 3, pp. 1982–1993, Mar. 2023, doi: 10.1109/TCYB.2022.3195355.

[4] Y. Cheng, N. Zhou, Z. Wang, B. Chen, and W. Zhang, "CFFsBD: A candidate fault frequencies-based blind deconvolution for rolling element bearings fault feature enhancement," *IEEE Trans. Instrum. Meas.*, vol. 72, pp. 1–12, 2023, doi: 10.1109/TIM.2023.3238032.

[5] M. Zhang, D. Wang, W. Lu, J. Yang, Z. Li, and B. Liang, "A deep transfer model with Wasserstein distance guided multi-adversarial networks for bearing fault diagnosis under different working conditions," *IEEE Access*, vol. 7, pp. 65303–65318, 2019.

[6] C. Li, L. Mo, and R. Yan, "Fault diagnosis of rolling bearing based on WHVG and GCN," *IEEE Trans. Instrum. Meas.*, vol. 70, pp. 1–11, 2021, doi: 10.1109/TIM.2021.3087834.

[7] L. Wen, X. Li, L. Gao, and Y. Zhang, "A new convolutional neural network-based data-driven fault diagnosis method," *IEEE Trans. Ind. Electron.*, vol. 65, no. 7, pp. 5990–5998, Jul. 2018, doi: 10.1109/TIE.2017.2774777.

[8] W. Mao, J. Liu, J. Chen, and X. Liang, "An interpretable deep transfer learning-based remaining useful life prediction approach for bearings with selective degradation knowledge fusion," *IEEE Trans. Instrum. Meas.*, vol. 71, pp. 1–16, 2022, doi: 10.1109/TIM.2022.3159010.

[9] T. Zhang, J. Chen, F. Li, K. Zhang, H. Lv, S. He, and E. Xu, "Intelligent fault diagnosis of machines with small & imbalanced data: A state-of-the-art review and possible extensions," *ISA Trans.*, vol. 119, pp. 152–171, Jan. 2022.

[10] Y. Su, L. Meng, X. Kong, T. Xu, X. Lan, and Y. Li, "Small sample fault diagnosis method for wind turbine gearbox based on optimized generative adversarial networks," *Eng. Failure Anal.*, vol. 140, Oct. 2022, Art. no. 106573.

[11] Z. Wu, W. Lin, B. Fu, J. Guo, Y. Ji, and M. Pecht, "A local adaptive minority selection and oversampling method for class-imbalanced fault diagnostics (don't short) in industrial systems," *IEEE Trans. Rel.*, vol. 69, no. 4, pp. 1195–1206, Dec. 2020.

[12] I. Martin-Diaz, D. Morinigo-Sotelo, O. Duque-Perez, and R. de J. Romero-Troncoso, "Early fault detection in induction motors using AdaBoost with imbalanced small data and optimized sampling," *IEEE Trans. Ind. Appl.*, vol. 53, no. 3, pp. 3066–3075, May 2017.

[13] Z. An, X. Jiang, J. Cao, R. Yang, and X. Li, "Self-learning transferable neural network for intelligent fault diagnosis of rotating machinery with unlabeled and imbalanced data," *Knowl.-Based Syst.*, vol. 230, Oct. 2021, Art. no. 107374.

[14] Y. Tan, L. Guo, H. Gao, Z. Lin, and Y. Liu, "MiDAN: A framework for cross-domain intelligent fault diagnosis with imbalanced datasets," *Measurement*, vol. 183, Oct. 2021, Art. no. 109834.

[15] N. Lu and T. Yin, "Transferable common feature space mining for fault diagnosis with imbalanced data," *Mech. Syst. Signal Process.*, vol. 156, Jul. 2021, Art. no. 107645.

[16] J. Wu, Z. Zhao, C. Sun, R. Yan, and X. Chen, "Few-shot transfer learning for intelligent fault diagnosis of machine," *Measurement*, vol. 166, Dec. 2020, Art. no. 108202.

[17] Y. Kaya, F. Kuncan, and H. M. Ertunç, "A new automatic bearing fault size diagnosis using time-frequency images of CWT and deep transfer learning methods," *Turkish J. Electr. Eng. Comput. Sci.*, vol. 30, no. 5, pp. 1851–1867, Jul. 2022.

[18] J. Gu, Y. Peng, H. Lu, X. Chang, and G. Chen, "A novel fault diagnosis method of rotating machinery via VMD, CWT and improved CNN," *Measurement*, vol. 200, Aug. 2022, Art. no. 111635.

[19] Y. Xu, Z. Li, S. Wang, W. Li, T. Sarkodie-Gyan, and S. Feng, "A hybrid deep-learning model for fault diagnosis of rolling bearings," *Measurement*, vol. 169, Feb. 2021, Art. no. 108502.

[20] J. Gu, Y. Peng, H. Lu, X. Chang, and G. Chen, "A novel fault diagnosis method of rotating machinery via VMD, CWT and improved CNN," *Measurement*, vol. 200, Aug. 2022, Art. no. 111635.

[21] I. J. Goodfellow, J. Pouget-Abadie, M. Mirza, B. Xu, D. Warde-Farley, S. Ozair, A. Courville, and Y. Bengio, "Generative adversarial nets," in *Proc. Neural Inf. Process. Syst.* Cambridge, MA, USA: MIT Press, 2014, pp. 139–144.

[22] W. Fang, F. Zhang, Y. Ding, and J. Sheng, "A new sequential image prediction method based on LSTM and DCGAN," *Comput., Mater. Continua*, vol. 64, no. 1, pp. 217–231, 2020.

[23] W. Fang, F. Zhang, V. S. Sheng, and Y. Ding, "A method for improving CNN-based image recognition using DCGAN," *Comput., Mater. Continua*, vol. 57, no. 1, pp. 167–178, 2018.

[24] J. Viola, Y. Chen, and J. Wang, "FaultFace: Deep convolutional generative adversarial network (DCGAN) based ball-bearing failure detection method," in *Proc. 1st Int. Conf. Ind. Artif. Intell. (IAI)*, Jul. 2019, pp. 1–6, doi: 10.1109/ICIAI.2019.8850805.

[25] Q. Guo, Y. Li, Y. Song, D. Wang, and W. Chen, "Intelligent fault diagnosis method based on full 1-D convolutional generative adversarial network," *IEEE Trans. Ind. Informat.*, vol. 16, no. 3, pp. 2044–2053, Mar. 2020, doi: 10.1109/TII.2019.2934901.

[26] M. T. Pham, J.-M. Kim, and C. H. Kim, "Rolling bearing fault diagnosis based on improved GAN and 2-D representation of acoustic emission signals," *IEEE Access*, vol. 10, pp. 78056–78069, 2022, doi: 10.1109/ACCESS.2022.3193244.

[27] Q. Mao, X. Yang, R. Zhang, G. Jeon, F. Hussain, and K. Liu, "Multi-focus images fusion via residual generative adversarial network," *Multimedia Tools Appl.*, vol. 81, no. 9, pp. 12305–12323, Apr. 2022.

[28] M. Zhao, S. Zhong, X. Fu, B. Tang, and M. Pecht, "Deep residual shrinkage networks for fault diagnosis," *IEEE Trans. Ind. Informat.*, vol. 16, no. 7, pp. 4681–4690, Jul. 2020.

[29] Z. Tong, W. Li, B. Zhang, F. Jiang, and G. Zhou, "Bearing fault diagnosis under variable working conditions based on domain adaptation using feature transfer learning," *IEEE Access*, vol. 6, pp. 76187–76197, 2018, doi: 10.1109/ACCESS.2018.2883078.

[30] Z. Zhang, H. Li, L. Chen, and P. Han, "Rolling bearing fault diagnosis using improved deep residual shrinkage networks," *Shock Vib.*, vol. 2021, pp. 1–11, May 2021.

[31] A. Salimy, I. Mitiche, P. Boreham, A. Nesbitt, and G. Morison, "Dynamic noise reduction with deep residual shrinkage networks for online fault classification," *Sensors*, vol. 22, no. 2, p. 515, Jan. 2022.

[32] Y. Peng, Y. Wang, and Y. Shao, "A novel bearing imbalance fault-diagnosis method based on a Wasserstein conditional generative adversarial network," *Measurement*, vol. 192, Mar. 2022, Art. no. 110924.

[33] W. Li, X. Zhong, H. Shao, B. Cai, and X. Yang, "Multi-mode data augmentation and fault diagnosis of rotating machinery using modified ACGAN designed with new framework," *Adv. Eng. Informat.*, vol. 52, Apr. 2022, Art. no. 101552.

[34] F. Nielsen, "On a generalization of the Jensen–Shannon divergence and the Jensen–Shannon centroid," *Entropy*, vol. 22, no. 2, p. 221, Feb. 2020.

[35] X. Mao, Q. Li, H. Xie, R. Y. K. Lau, Z. Wang, and S. P. Smolley, "Least squares generative adversarial networks," in *Proc. IEEE Int. Conf. Comput. Vis. (ICCV)*, Oct. 2017, pp. 2813–2821.

[36] M. Arjovsky, S. Chintala, and L. Bottou, "Wasserstein GAN," Tech. Rep., 2017, doi: 10.48550/arXiv.1701.07875.

[37] I. Gulrajani, F. Ahmed, M. Arjovsky, V. Dumoulin, and A. Courville, "Improved training of Wasserstein GANs," 2017, *arXiv:1704.00028*, doi: 10.48550/arXiv.1704.00028.

[38] R. Pascanu and Y. Bengio, "Revisiting natural gradient for deep networks," 2013, *arXiv:1301.3584*.

[39] K. He, X. Zhang, S. Ren, and J. Sun, "Deep residual learning for image recognition," in *Proc. IEEE Conf. Comput. Vis. Pattern Recognit. (CVPR)*, Las Vegas, NV, USA, Jun. 2016, pp. 770–778, doi: 10.1109/CVPR.2016.90.

[40] M. Tan, B. Chen, R. Pang, V. Vasudevan, M. Sandler, A. Howard, and Q. V. Le, "MnasNet: Platform-aware neural architecture search for mobile," in *Proc. IEEE/CVF Conf. Comput. Vis. Pattern Recognit. (CVPR)*, Long Beach, CA, USA, Jun. 2019, pp. 2815–2823, doi: 10.1109/CVPR.2019.00293.

[41] H. Zhang, K. Zu, J. Lu, Y. Zou, and D. Meng, "EPSANet: An efficient pyramid squeeze attention block on convolutional neural network," in *Proc. 16th Asian Conf. Comput. Vis. (ACCV)*, Macao, China. Berlin, Germany: Springer-Verlag, 2023, pp. 541–557, doi: 10.1007/978-3-031-26313-2_33.

[42] W. Mao, Y. Liu, L. Ding, and Y. Li, "Imbalanced fault diagnosis of rolling bearing based on generative adversarial network: A comparative study," *IEEE Access*, vol. 7, pp. 9515–9530, 2019.

[43] W. Qian and S. Li, "A novel class imbalance-robust network for bearing fault diagnosis utilizing raw vibration signals," *Measurement*, vol. 156, May 2020, Art. no. 107567.

ZHIDAN ZHONG received the Ph.D. degree in control theory and control engineering from Shanghai Jiao Tong University, in 2007. He is currently a Professor with the School of Mechanical and Electrical Engineering, Henan University of Science and Technology, China. His primary research interests include electromechanical systems measurement and control, intelligent bearing technology, and digital twin testing. He serves as the Deputy Director for the Mechanical and Electronic Engineering Discipline Committee, China Mechanical Industry Education Association.

HAO LIU received the bachelor's degree in mechanical design, manufacturing and automation from the Henan University of Technology, in 2016. He is currently pursuing the master's degree in mechanical engineering with the Henan University of Science and Technology. His main research interests include machine learning, signal processing, and fault diagnosis.

WENTAO MAO (Member, IEEE) received the M.S. degree in computer science from the Chongqing University of Posts and Telecommunications, Chongqing, China, in 2006, and the Ph.D. degree in engineering mechanics from Xi'an Jiaotong University, Xi'an, China, in 2011. He is currently a Full Professor with the School of Computer and Information Engineering, Henan Normal University, Xinxiang, China. He has conducted and is conducting about ten research projects, such as the National Natural Science Foundation of China as a Project Principal or a Main Researcher. His current research interests include machine learning, time series analysis, and fault prognostics.

XINGHUI XIE received the bachelor's degree from the Henan University of Science and Technology, in 1993. He currently serves as a Senior Engineer at the State Key Laboratory of Aerospace Precision Bearings, Luoyang. He has been actively engaged in the design and research of bearing products for an extended period of time. He has led the development of various new bearing products, widely applied across various sectors of the national economy. Additionally, he is dedicated to the localization and substitution of imported bearings.

WENLU HAO received the bachelor's degree from the Henan University of Science and Technology, in 1987. He was the Chief Engineer with Luoyang Xinqiang Rotary Bearing Company Ltd. He has led three projects at the provincial level or above. His research interests include the design, manufacturing, and application technology of wind turbine bearings. He received one second-class prize in the Henan Province's Science and Technology Progress Award as well as two second-class prizes in the Mechanical Industry Award.

YUNHAO CUI was born in 1986. He received the Ph.D. degree in engineering from the Dalian University of Technology. He is mainly engaged in the research of intelligent construction machinery, intelligent bearing inspection, 3D point cloud-based operating environment perception, and image machine vision.